

# Electroproduction of $\Lambda(1520)$ off the nucleon target with $D_{13}(2150)$

Seung-il Nam\*

*School of Physics, Korea Institute for Advanced Study (KIAS), Seoul 130-722, Republic of Korea*

(Dated: June 18, 2022)

We investigate the electroproduction of  $\Lambda(1520) \equiv \Lambda^*$  off the nucleon target, using the effective Lagrangian method at the tree-level Born approximation with the dominant nucleon-resonance contribution from  $D_{13}(2150)$ . First, we compute the various physical quantities for the proton target case, such as the total and differential cross sections,  $t$ -momentum transfer distribution, and  $K^-$  decay-angle ( $\phi$ ) distribution. It turns out that the  $D_{13}(2150)$  plays an important role to reproduce the electroproduction data correctly. The numerical results for the  $\phi$  distribution shows obvious different structures from that for the photoproduction, due to the enhancement of the kaon exchange by the longitudinal polarization of the virtual photon as expected. Numerically, we observe that the kaon-exchange contribution in the  $t$  channel becomes about a half of that from the contact-term one that dominates the photoproduction of  $\Lambda^*$ . We also provide theoretical estimations for the  $\Lambda^*$  electroproduction off the neutron target, showing that its production rate is saturated almost by the resonance contribution. Finally, the contact-term dominance, which is the key ingredient for the  $\Lambda^*$  electromagnetic productions, is briefly discussed.

PACS numbers: 11.10.Ef, 13.30.Eg, 13.60.-r, 14.20.Gk, 14.20.Jn.

Keywords: Electroproduction of  $\Lambda(1520)$ , effective Lagrangian approach,  $D_{13}(2150)$  resonance, decay-angle distribution, contact-term dominance.

## I. INTRODUCTION

Photo and electroproductions, i.e. electromagnetic (EM) productions of the hadrons off the nucleon target has been an very useful tool to study the nonperturbative quantum chromodynamics (QCD) in terms of the color-singlet degrees of freedom at a scale  $\sim 1$  GeV from the experimental and theoretical points of view. By doing that, one can extract the fundamental information for the EM and strong interaction structures, the hadron mass spectra, and missing resonances searches for instance. Note that the EM production of hadrons have been studied energetically by the various experimental collaborations: LAMP2 at Daresbury [1], CLAS at Jefferson Laboratory [2], LESP at SPring-8 [3–5], CB-ELSA/TAPS at Bonn [6], and so on. Along with those experimental endeavors, there have been abundant theoretical works for them as well, such as the photoproduction of  $K\Lambda(1520)$  [7–12],  $\eta N$  [13],  $\pi\Delta(1231)$  [14],  $K\Lambda(1116)$  [15],  $K^*\Lambda(1116)$  [16, 17], and  $K^*\Sigma(1190)$  [18], employing the tree-level Born approximation with the effective Lagrangian approach, and accumulated considerably important results. Among those theoretical efforts, it is worth mentioning the interesting results of our previous works on the  $\Lambda(1520, 3/2^-) \equiv \Lambda^*$  photoproduction [7, 9, 10]. In terms of the gauge invariance of the scattering amplitude, i.e. the Ward-Takahashi (WT) identity, it turned out that the contact-term contribution prevails over all other kinematic channels. This interesting behavior of the *contact-term dominance* can be also resulted in the large target asymmetry, saying that the production rate from the proton target is much larger than that for the neutron-target case, in which the contact-term contribution does not exists due to the electric-charge conservation:  $\sigma_n \ll \sigma_p$ . In 2009, the LEPS collaboration reported that the differential cross sections for the  $\Lambda^*$  photoproduction off the proton as well as the deuteron targets. Interestingly enough, the production rates turned out to be similar to each other:  $d\sigma_d/d\cos\theta \sim d\sigma_p/d\cos\theta$ . Here,  $\theta$  denotes the angle for the outgoing  $K^+$  with respect to the incident photon in the center-of-mass (cm) system. Thus, this observation indicates that the contact-term dominance works qualitatively well, if we take into account a naive but reasonable assumption  $\sigma_d \sim \sigma_p + \sigma_n$  [3]. Note that there are theoretical supports for the contact-term dominance for  $\gamma p \rightarrow K^+\Lambda^*$  [5, 8].

The resonance contributions for the  $\Lambda^*$  production is also important to be studied. From the photoproduction experiment by the LEPS collaboration [4], it was observed that the peak of the differential cross section as a function of  $E_\gamma$  varies its strength depending on the  $\theta$  angle. This tendency may indicate a possible contribution from a nucleon resonance. Then, the two theoretical works, employing the effective approaches, suggested that the  $D_{13}(2080)$  resonance, which is now split into two different resonant states  $D_{13}(2120)$  and  $D_{13}(1875)$  [19], can be the most possible candidate for it [11, 12]. We also want to focus on the distinctive features between the electro and photoproductions

---

\*E-mail: sinam@kias.re.kr

of  $\Lambda^*$ . In the CLAS experiment for the  $\Lambda^*$  electroproduction [2], the  $K^-$  decay-angle ( $\phi$ ) distribution in the Gottfried-Jackson (GJ) frame was described mainly by a curve  $\propto (1/3 + \cos^2 \phi)$ , signaling that  $\Lambda^*(S = 1/2)$  decays into  $K^-p$  mainly, in addition to small contributions from the other spin states. Here,  $\Lambda^*(S)$  stand for that  $\Lambda^*$  in its spin- $S$  states, and  $\phi$  indicates the angle between the target nucleon and outgoing  $K^-$  in the  $\Lambda^*$  rest frame. In contrast, the  $\phi$  distribution for the  $\Lambda^*$  photoproduction shows the curve  $\propto \sin^2 \phi$ , in which  $\Lambda^*(S = 3/2)$  decay into  $K^-p$  [1, 3]. In our previous work [10], the  $\phi$  distribution for the photoproduction was reproduced qualitatively well in terms of the contact-term dominance. This result also indicates that the contact-term contribution plays the role of the spin-1 meson exchange in addition to the  $K^*$  exchange in the  $t$  channel. In general, the most obvious difference in these two EM productions is that the existence of the longitudinal-polarization component of the virtual photon. Physically, the difference shown in the  $\phi$  distribution between the EM productions can be understood by the  $S_z = 0$  (longitudinal) component of the polarization vector selects the spin-0 meson, i.e. kaon exchange in the  $t$  channel. Hence, in the electroproduction, the possibility for  $\Lambda^*(S = 1/2)$  gets enhanced than that for  $\Lambda^*(S = 3/2)$ , resulting in that the curve shape for the  $\phi$  distribution becomes proportional to  $\propto (1/3 + \cos^2 \phi)$ .

Focusing on the two intriguing ingredients mentioned above, 1) the nucleon-resonance contribution and 2) the distinctive features in the electroproduction in comparison to the photoproduction, in the present work, we want to investigate the elementary process for the electroproduction of  $\Lambda(1520, 3/2^-) \equiv \Lambda^*$  off the nucleon target, i.e.  $\gamma^*N \rightarrow K\Lambda^*$ . So far, we have had only one  $\Lambda^*$ -electroproduction experiment done by Barrow *et al.* of the CLAS collaboration [2]. Hence, we will closely explore those data theoretically in the present work. To this end, we make use of the effective Lagrangian approach at the tree-level Born approximation, closely following the theoretical framework in our previous works [7, 9, 10]. The Rarita-Schwinger vector-spinor formalism is employed for describing the spin-3/2 field for  $\Lambda^*$  in a field theoretical manner [20, 21]. We also take into account the phenomenological form factors for each kinematic channels, following the prescription suggested in Refs. [22–24], with a newly devised gauge-conserving term similar to that given in Ref. [25]. All the numerical calculations are performed in the  $K$ - $\Lambda^*$  cm system with the properly defined four momenta and polarization vectors for the relevant particles involved. The transverse polarization parameter  $\varepsilon$  is chosen to be 0.5 throughout the theoretical calculations, considering the experimentally given value  $\varepsilon = (0.3 \sim 0.7)$  [2]. In addition, taking into account the CLAS experiment, we choose the kinematic regions for the photon virtuality and  $K$ - $\Lambda^*$  cm energy as  $Q^2 = (0.9 \sim 2.4) \text{ GeV}^2$  and  $W = (1.95 \sim 2.65) \text{ GeV}$ , respectively. In the present work, as a first step to investigate the nucleon-resonance effects for the scattering process, we take into account  $D_{13}(2150)$ , which was considered  $D_{13}(2080)$  before as mentioned above [19], since this resonance was found to be relevant in the  $\Lambda^*$  photoproduction [11, 12]. In order to study the  $\phi$  distribution, we devise a simple parameterization for it, by separating the differential cross section into each spin states theoretically [10].

Firstly, as for the theoretical results, we provide the total and differential cross sections,  $\Lambda^*$  spin distribution,  $\phi$  distribution, and  $t$ -momentum transfer distribution for the proton target case. It turns out that the present theoretical framework reproduces the data qualitatively very well with the resonance contribution, which plays a crucial role in the vicinity of  $W \approx 2.1 \text{ GeV}$ . At the same time, it turns out that the  $D_{13}(2150)$  resonance enhances the production rate in the forward-scattering region. We also show numerically that the longitudinal-polarization of the virtual photon enhances the kaon-exchange contribution more as expected, than its effects on the contact-term one. This enhancement is also shown explicitly by that the numerical results for the  $\phi$  distribution turns out to be considerably different from that for the photoproduction. Secondly, we apply the determined information for  $D_{13}(2150)$  from the electroproduction to the photoproduction of  $\Lambda^*$  to see the effects of the  $D_{13}(2150)$  resonance. By doing that, we observe that the resonance contribution is not so effective in comparison to that for the electroproduction, since the contact-term contribution dominates the photoproduction process even with the resonance. Finally, using all the ingredients obtained above, we compute the total and differential cross sections for the  $\Lambda^*$  electroproduction off the neutron target, with a rough estimation for the EM interaction strengths for  $D_{13}(2150)$ . On top of the negligible  $K^*$ -exchange contribution, the production rate of the cross sections are reproduced almost by the  $D_{13}(2150)$  resonance, although it is hard to reproduce the experimental data correctly only with the single nucleon resonance. From this, we can conclude that the  $\Lambda^*$  EM productions off the neutron target are utmost useful production channels to investigate the nucleon-resonance contributions, since the production rate is dominated almost only by them, according to the *contact-term dominance*. Moreover, we make some brief comments on the contact-term dominance in the  $\Lambda^*$  EM productions, considering all the observations mentioned above.

The present work is organized as follows: In Section II, we briefly introduce the present theoretical framework, defining the effective interactions for the relevant Yukawa vertices, computing coupling strengths, writing down the invariant amplitudes, and so on. The numerical results and related discussions are given in Section III. Section IV is devoted for summary and future prospectives.

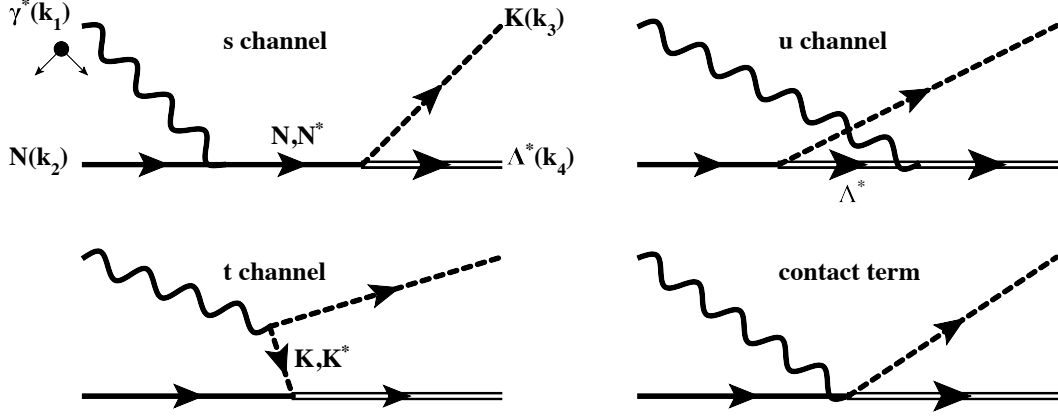


FIG. 1: Tree-level Feynman diagrams for  $\gamma^* N \rightarrow K \Lambda^*$ . Relevant momenta of the particles involved are defined in Eq. (1).

## II. THEORETICAL FRAMEWORK

In this Section, we introduce the theoretical framework to compute the  $\Lambda^*$  electroproduction off the nucleon target. We note that all the calculations are performed in the  $K$ - $\Lambda^*$  cm frame, where the four momenta of the particles, depicted in Figs. 1 for  $\gamma^* N \rightarrow K \Lambda^*$  and 2 for  $e N \rightarrow e' K \Lambda^*$ , are defined as follows:

$$k_1 = (E_1, 0, 0, k), \quad k_2 = (E_2, 0, 0, -k), \quad k_3 = (E_3, p \sin \theta, 0, p \cos \theta), \quad k_4 = (E_4, -p \sin \theta, 0, -p \cos \theta), \quad (1)$$

where  $k_1, k_2, k_3$ , and  $k_4$  stand for the four momenta for the incident virtual photon, target nucleon, outgoing kaon, and recoil  $\Lambda^*$ , and the same for their masses  $M_{1\sim 4}$ , i.e.  $M_{1,2,3,4} = M_{\gamma, N, K, \Lambda^*}$ .  $\theta$  for the angle between the photon and the kaon in the cm frame. As understood, the reaction plane is defined by the  $x$ - $z$  plane, whereas  $z$  direction is set to be parallel to the incident virtual photon three momentum: Considering the azimuthal symmetry, we set the azimuthal angle  $\varphi$  in Figure 2 to be zero. In the electroproduction, there are two *independent* kinematic variables  $W^2$  and  $Q^2$ , which are defined by  $W^2 = (k_1 + k_2)^2 = (k_3 + k_4)^2$  and  $Q^2 = -k_1^2 > 0$ , respectively. Hereafter, we employ a notation  $\sqrt{Q^2} \equiv Q$  for convenience. Using these variables, the energies of the particles can be written by

$$E_1 = \frac{W^2 - Q^2 - M_2^2}{2W}, \quad E_2 = \frac{W^2 + Q^2 + M_2^2}{2W}, \quad E_3 = \frac{W^2 - M_{\Lambda^*}^2 + M_3^2}{2W}, \quad E_4 = \frac{W^2 + M_4^2 - M_3^2}{2W}. \quad (2)$$

Here, we write the absolute values for the three momenta for the initial- and final-state particles:

$$k = \sqrt{E_1^2 + Q^2}, \quad p = \sqrt{E_3^2 - M_3^2}. \quad (3)$$

Now, we are in a position to define the frame-independent transverse-polarization parameter  $\varepsilon$ , which measures the strength of the transverse polarization in the virtual photon:

$$\varepsilon = \left[ 1 + \frac{2k_1^2}{Q^2} \tan^2 \left( \frac{\Psi}{2} \right) \right]^{-1}, \quad (4)$$

where  $\Psi$  denotes the polar angle for the electron for  $e N \rightarrow e' K \Lambda^*$  as depicted in Figure 2. Using  $\varepsilon$ , the photon-polarization vectors, two transverse ( $x, y$ ) and one longitudinal ( $z$ ), are given as follows [26]:

$$\epsilon_x = (0, 0, \sqrt{1 - \varepsilon}, 0), \quad \epsilon_y = (0, \sqrt{1 + \varepsilon}, 0, 0), \quad \epsilon_z = \frac{\sqrt{2\varepsilon}}{Q} (k, 0, 0, E_1). \quad (5)$$

As shown in Ref. [26], the scalar (0-th) components of the scattering amplitude can be omitted by virtue of the gauge invariance (WT identity). According to this, the photon-polarization vectors can be modified into three vectors by omitting the 0-th component and multiplying a factor  $k_1^2/E_1^2$ , resulting in  $\varepsilon \rightarrow \varepsilon_L \equiv (Q^2/E_1^2)\varepsilon$  (see Appendix). We, however, do not consider this treatment in the present work, keeping all the Lorentz components intact in the calculations, satisfying the WT identity explicitly. For more details for the electroproduction of pseudoscalar mesons, one can refer Refs. [27–31].

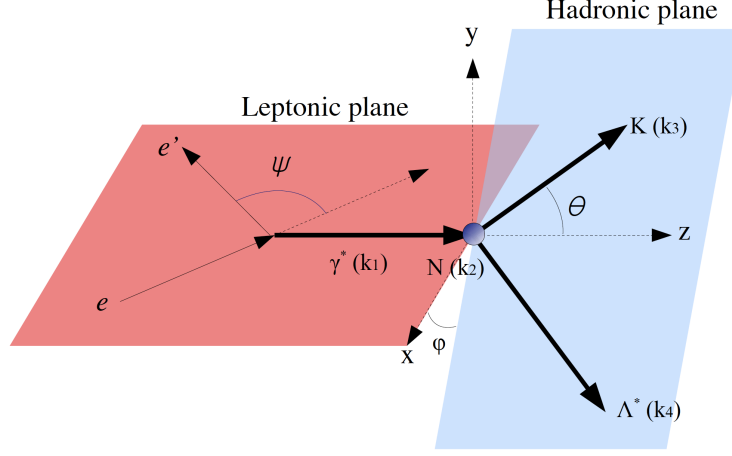


FIG. 2: Definition of the leptonic and hadronic reaction planes for  $eN \rightarrow e'K\Lambda^*$ . Note that  $\varphi$  indicates the azimuthal angle.

The effective Lagrangians for the EM and strong interaction vertices are defined by

$$\begin{aligned}
\mathcal{L}_{\gamma KK} &= ie_K [(\partial^\mu K^\dagger)K - (\partial^\mu K)K^\dagger] A_\mu + \text{h.c.}, \\
\mathcal{L}_{\gamma NN} &= -\bar{N} \left[ e_N \not{A} - \frac{e_Q \kappa_N}{4M_N} \sigma \cdot F \right] N + \text{h.c.}, \\
\mathcal{L}_{\gamma \Lambda^* \Lambda^*} &= -\bar{\Lambda}^{*\mu} \left[ \left( -F_1 \not{\epsilon} g_{\mu\nu} + F_K \not{\epsilon} \frac{k_{1\mu} k_{1\nu}}{2M_{\Lambda^*}^2} \right) - \frac{\not{k}_1 \not{\epsilon}}{2M_{\Lambda^*}} \left( -F_2 g_{\mu\nu} + F_4 \frac{k_{1\mu} k_{1\nu}}{2M_{\Lambda^*}^2} \right) \right] \Lambda^{*\nu} + \text{h.c.}, \\
\mathcal{L}_{\gamma KK^*} &= g_{\gamma KK^*} \epsilon_{\mu\nu\sigma\rho} (\partial^\mu A^\nu) (\partial^\sigma K) K^{*\rho} + \text{h.c.}, \\
\mathcal{L}_{\gamma K N \Lambda^*} &= -\frac{ie_N g_{KN\Lambda^*}}{M_{\Lambda^*}} \bar{\Lambda}^{*\mu} A_\mu K \gamma_5 N + \text{h.c.}, \\
\mathcal{L}_{KN\Lambda^*} &= \frac{g_{KN\Lambda^*}}{M_{\Lambda^*}} \bar{\Lambda}^{*\mu} \partial_\mu K \gamma_5 N + \text{h.c.}, \\
\mathcal{L}_{K^* N \Lambda^*} &= -\frac{iG_1}{M_V} \bar{\Lambda}^{*\mu} \gamma^\nu G_{\mu\nu} N - \frac{G_2}{M_V^2} \bar{\Lambda}^{*\mu} G_{\mu\nu} \partial^\nu N + \frac{G_3}{M_V^2} \bar{\Lambda}^{*\mu} \partial^\nu G_{\mu\nu} N + \text{h.c.}
\end{aligned} \tag{6}$$

Here, the  $e_h$  and  $e_Q$  denote the electric charge of the hadron  $h$  and unit electric charge, respectively. The  $A$ ,  $K$ ,  $K^*$ ,  $N$ , and  $\Lambda^*$  indicate the fields for the photon, kaon, vector kaon, nucleon, and  $\Lambda^*$ . As for the spin-3/2 fermion field, we employ of the Rarita-Schwinger (RS) vector-spinor field [20, 21]. We also make use of the notation  $\sigma \cdot F = \sigma_{\mu\nu} F^{\mu\nu}$ , where  $\sigma_{\mu\nu} = i(\gamma_\mu \gamma_\nu - \gamma_\nu \gamma_\mu)/2$  and the EM field strength tensor  $F^{\mu\nu} = \partial^\mu A^\nu - \partial^\nu A^\mu$ . The  $\kappa_{N,\Lambda^*}$  denote the anomalous magnetic momentum for the nucleon and the  $\Lambda^*$ . Although the spin-3/2  $\Lambda^*$  has four different electromagnetic form factors  $F_{1,2,3,4}$  as shown in Eq. (6) in general, we only take into account the dipole one ( $F_2 \equiv e_Q \kappa_{\Lambda^*}$ ) as a free parameter, since we do not have any theoretical and experimental information for it, ignoring the monopole ( $F_1 \equiv e_{\Lambda^*} = 0$ ), quadrupole ( $F_3$ ), and octupole ( $F_4$ ) ones, since their contributions are assumed to be negligible. As a trial, we will choose  $\kappa_{\Lambda^*} \sim \kappa_n$  in the present work. Using the  $\gamma KK^*$  interaction given in Eq. (6) and experimental data [32], one obtains that  $g_{\gamma K^* \pm K^\mp} = 0.254/\text{GeV}$  and  $g_{\gamma K^* 0 K^0} = 0.358/\text{GeV}$ . The  $g_{KN\Lambda^*}$  can be computed with the experimental data for the full and partial decay widths:  $\Gamma_{\Lambda^*} \approx 15.6 \text{ MeV}$  and  $\Gamma_{\Lambda^* \rightarrow \bar{K} N}/\Gamma_{\Lambda^*} \approx 0.45$  [32], resulting in that  $g_{KN\Lambda^*} \approx 11$ . As for the  $K^* N \Lambda^*$  interaction, there are three individual terms, and we defined a notation  $G_{\mu\nu} = \partial_\mu K_\nu^* - \partial_\nu K_\mu^*$ . Since we have only insufficient experimental and theoretical [33] information to determine all the coupling strengths for the  $G_{1,2,3}$ , we set  $G_2$  and  $G_3$  to be zero for simplicity. We will take the value for  $G_1 \equiv g_{K^* N \Lambda^*}$  from the theoretical estimation using the coupled chiral unitary approach, resulting in  $|g_{K^* N \Lambda^*}| \approx 1.5$  [33].

Since we are interested in the nucleon resonance  $D_{13}(2150, 3/2^-)$ , which was denoted by  $D_{13}(2080)$  before in PDG [19] and suggested to give a considerable contribution to the  $\Lambda^*$  photoproduction [4, 11, 12], we write the effective Lagrangians for the  $s$ -channel diagram for  $D_{13}$ :

$$\begin{aligned}
\mathcal{L}_{\gamma NR} &= -\frac{ie_Q h_1}{2M_N} \bar{R}_\mu \gamma_\nu F^{\mu\nu} N - \frac{e_Q h_2}{(2M_N)^2} \bar{R}_\mu F^{\mu\nu} (\partial_\nu N) + \text{h.c.}, \\
\mathcal{L}_{KR\Lambda^*} &= \frac{g_1}{M_K} \bar{\Lambda}^{*\mu} \gamma_5 (\not{\partial} K) R^\mu + \frac{ig_2}{M_K^2} \bar{\Lambda}^{*\mu} \gamma_5 (\partial_\mu \partial_\nu K) R^\nu + \text{h.c.},
\end{aligned} \tag{7}$$

where  $R$  stands for the resonance field. Again, we employed the RS formalism here for it. Here is a comment: In PDG of 2012 [19], the resonance mass was assigned to be 2120 MeV as an average value, whereas Ref. [34] wrote it with 2150 MeV. In the present work, since we will use the values for the helicity amplitude for the resonance, which will be used for numerical calculations, from Ref. [34], we choose  $M_R = 2150$  MeV through this work. The  $h_{1,2}$  and  $g_{1,2}$  denote the EM transition couplings corresponding to the helicity amplitudes  $A_{1/2}$  and  $A_{3/2}$ , and strong coupling constants. To obtain the values for those couplings, we refer to the experimental data and SU(6) quark-model estimations [19, 34, 35], and the input values are listed in Table I. The helicity amplitude for the decay  $R \rightarrow \gamma N$  is given by

$$A_{1/2}^{R \rightarrow \gamma N} = \frac{e_Q \sqrt{6}}{12} \sqrt{\frac{k_\gamma}{M_N M_R}} \left[ h_1 + \frac{h_2}{4M_N^2} M_R (M_R + M_N) \right], \quad A_{3/2}^{R \rightarrow \gamma N} = \frac{e_Q \sqrt{2}}{4M_N} \sqrt{\frac{k_\gamma M_R}{M_N}} \left[ h_1 + \frac{h_2}{4M_N} (M_R + M_N) \right]. \quad (8)$$

Using the input values for the helicity amplitudes [34], we have the followings for the proton, ignoring the errors:

$$h_1^{p*} = -0.73, \quad h_2^{p*} = 2.02. \quad (9)$$

Note that these values are quite different in comparison to those computed from the old data [32], giving  $h_1^{p*} = 0.608$  and  $h_2^{p*} = -0.620$  with  $M_R = 2080$  MeV. As for the strong coupling for the  $KR\Lambda^*$  vertex, we have not had experimental as well as theoretical information yet. Instead, there were the SU(6) quark-model calculations for  $D_{13}(2080)$  [35]. Although we will treat  $g_1$  as a *free* parameter to reproduce the experimental data, considering the present situation, we can make use of this theoretical information as a guide to estimate  $g_1$  realistically. The partial decay amplitude for  $R \rightarrow K\Lambda^*$  is related to the  $G(\ell)$  through the following equation [35]:

$$\Gamma_{R \rightarrow K\Lambda^*} = \sum_{\ell} |G(\ell)|^2. \quad (10)$$

Since we are interested in the low-energy region near the threshold, i.e.  $k_K \ll M_K$ , we rather safely ignore the second term proportional to  $g_2$  in Eq. (7) [17]. Employing the following equation for determining the strong coupling [8]

$$\Gamma_{R \rightarrow K\Lambda^*} = \frac{g_1^2 q M_R (E_{\Lambda^*} - M_{\Lambda^*})}{18\pi M_{\Lambda^*}^2 M_R^2} \left[ \frac{M_R + M_{\Lambda^*}}{M_R} \right]^2 \left[ E_{\Lambda^*}^2 - E_{\Lambda^*} M_{\Lambda^*} + \frac{5}{2} M_{\Lambda^*}^2 \right], \quad (11)$$

where the absolute value for the three momentum for the decaying particle can be computed by the Källén function

$$q = \frac{\sqrt{[M_R^2 - (M_{\Lambda^*} + M_K)^2][M_R^2 - (M_{\Lambda^*} - M_K)^2]}}{2M_R}, \quad (12)$$

and using the values in Table I, we have the following by considering the theoretical errors:  $|g_1| = (0 \sim 1.52)$  and  $g_2 \rightarrow 0$ , where we used  $M_R = 2150$  MeV [34] and  $\Gamma_{R \rightarrow K\Lambda^*} \approx 7$  MeV [35]. Furthermore, since we can not determine the phase between the resonance contribution and the others, we will employ a phase factor as  $g_1 = |g_1| e^{i\phi_{\text{phase}}}$  for  $-\pi \leq \phi_{\text{phase}} \leq \pi$ . All the numerical values for the model parameters are given in Table II.

Using the effective Lagrangians given in Eqs. (6) and (7), one can straightforwardly evaluate the following invariant amplitudes, corresponding to the Feynman diagrams in Figure 1:

$$\begin{aligned} i\mathcal{M}_s^N &= -\frac{g_{KN\Lambda^*}}{M_K} \bar{u}_2^\mu k_{3\mu} \gamma_5 \left[ \frac{e_N [k_1 F_N(s) + (\not{k}_2 + M_N) F_c(s, t)]}{s - M_N^2} \not{\epsilon} - \frac{e_Q \kappa_p (\not{k}_1 + \not{k}_2 + M_N) F_N(s)}{2M_N (s - M_N^2)} \not{\epsilon} \not{k}_1 \right] u_1, \\ i\mathcal{M}_u^{\Lambda^*} &= -\frac{e_Q g_{KN\Lambda^*} \kappa_{\Lambda^*}}{2M_K M_{\Lambda^*}} \bar{u}_2^\mu (\not{k}_1 \not{\epsilon}) \left[ \frac{(\not{k}_4 - \not{k}_1 + M_{\Lambda^*})}{u - M_{\Lambda^*}^2} \right] k_{3\mu} \gamma_5 u_1 F_{\Lambda^*}(u), \\ i\mathcal{M}_t^K &= \frac{e_K g_{KN\Lambda^*}}{M_K} \bar{u}_2^\mu \left[ \frac{(k_{1\mu} - k_{3\mu}) [2(\epsilon \cdot k_3) F_c(s, t) - (\epsilon \cdot k_1) F_K(t)]}{t - M_K^2} \right] \gamma_5 u_1, \\ i\mathcal{M}_t^{K^*} &= -\frac{ig_{\gamma KK^*} g_{K^* NB}}{M_{K^*}} \bar{u}_2^\mu \gamma_\nu \left[ \frac{(k_1^\mu - k_3^\mu) g^{\nu\sigma} - (k_1^\nu - k_3^\nu) g^{\mu\sigma}}{t - M_{K^*}^2} \right] (\epsilon_{\rho\eta\xi\sigma} k_1^\rho \epsilon^\eta k_3^\xi) u_1 F_{K^*}(t), \end{aligned}$$

| $M_R$ [MeV]     | $\Gamma_R$ [MeV] | $A_{1/2}^{R \rightarrow \gamma p} [\frac{1}{\sqrt{\text{GeV}}}]$ | $A_{3/2}^{R \rightarrow \gamma p} [\frac{1}{\sqrt{\text{GeV}}}]$ | $\Gamma_{R \rightarrow K\Lambda^*}$ [MeV] | $G(1)$ [ $\sqrt{\text{MeV}}$ ] | $G(3)$ [ $\sqrt{\text{MeV}}$ ] |
|-----------------|------------------|--|--|---|--------------------------------|--------------------------------|
| $(2150 \pm 60)$ | $(330 \pm 45)$   | $0.125 \pm 0.045$  | $0.150 \pm 0.060$  | $6.76_{-6.76}^{+8.41}$ MeV                | $-2.6_{-2.8}^{+2.6}$           | $-0.2_{-1.3}^{+0.2}$           |

TABLE I: Input parameters for  $D_{13}(2120) \equiv R$  taken from Ref. [34] and theoretical estimations for  $KN^*\Lambda^*$  properties from the SU(6) quark model [35].

$$\begin{aligned}
i\mathcal{M}_{\text{contact}} &= \frac{e_K g_{K\Lambda^*}}{M_K} \bar{u}_2^\mu \epsilon_\mu \gamma_5 u_1 F_c(s, t), \\
i\mathcal{M}_{\text{gauge}} &= -\frac{g_{K\Lambda^*}}{M_K} \bar{u}_2^\mu \gamma_5 (\epsilon \cdot k_1) \left[ \frac{e_N k_{3\mu} [F_c(s, t) - F_N(s)]}{s - M_N^2} + \frac{e_K (k_{1\mu} - k_{3\mu}) [F_c(s, t) - F_K(t)]}{t - M_K^2} \right] u_1, \\
i\mathcal{M}_s^R &= -\frac{e_Q |g_1| e^{i\phi_{\text{phase}}}}{2M_K M_N} \bar{u}_2^\mu \frac{\gamma_5 \not{k}_3 (\not{k}_1 + \not{k}_2 + M_N) \mathcal{G}_{\mu\nu}}{s - M_R^2 + i\Gamma_R M_R} \left[ h_1 (k_1^\nu \not{\epsilon} - \not{k}_1 \epsilon^\nu) - \frac{h_2}{2M_N} [k_1^\nu (\epsilon \cdot k_2) - \epsilon^\nu (k_1 \cdot k_2)] \right] u_1 F_R(s).
\end{aligned} \tag{13}$$

The spin-3/2 projection operator can be written as follows:

$$\mathcal{G}_{\mu\nu}(q) = -g_{\mu\nu} + \frac{1}{3} \gamma_\mu \gamma_\nu + \frac{1}{3M_R} (\gamma_\mu q_\nu - \gamma_\nu q_\mu) + \frac{2}{3M_R^2} q_\mu q_\nu. \tag{14}$$

The sum of all the invariant amplitudes satisfy the gauge invariance (WT identity),  $k_1 \cdot \mathcal{M}_{\text{total}} = 0$ , with the phenomenological form factors  $F_h$ , following the gauge-conserving form-factor prescription suggested by Refs. [22–24]. Note that we have employed an additional term  $\mathcal{M}_{\text{gauge}}$  to conserve the gauge invariance of the scattering amplitude. This choice of  $\mathcal{M}_{\text{gauge}}$  is slightly different from the usual pseudoscalar meson electroproduction with the ground state baryons [25], in which a term proportional to  $(k_1 \cdot \epsilon)/Q^2$  is taken into account to save the gauge invariance. We, however, consider that the electroproduction scattering amplitude should be smoothly interpolated as  $Q^2 \rightarrow 0$  to that for the photoproduction, which is given in our previous work [7, 9, 10] and provided good agreement with experimental data [1, 3]. In this sense, we introduce the additional term,  $\mathcal{M}_{\text{gauge}}$  for the gauge invariance as in Eq. (13) from a phenomenological point of view. The form factors  $F_h$  are written by:

$$F_h(x) = \frac{\Lambda^4}{\Lambda^4 + (x - M_h^2)^2}, \tag{15}$$

where  $x$  denote the Mandelstam variables. The *common* form factor to conserve the on-shell condition, i.e. a form factor becomes unity at zero virtuality, is assigned by [7, 9, 10, 23]

$$F_c(s, t) = F_N(s) + F_K(t) - F_N(s)F_K(t). \tag{16}$$

The cutoff mass  $\Lambda$  will be determined to reproduce the experimental data in the next Section.

### III. NUMERICAL RESULTS

In this Section, we will provide and discuss various theoretical results for  $\gamma^* N \rightarrow K\Lambda^*$ . As for the experimental data to be compared with the numerical results, we will closely explore those from the experiment done by Barrow *et al.* of the CLAS collaboration [2]. In this experiment, the kinematical ranges for  $W$  and  $Q^2$  are  $(1.95 \sim 2.65)$  GeV and  $(0.9 \sim 2.4)$  GeV<sup>2</sup>, respectively. Moreover, the value of  $\varepsilon$ , defined in Eq. (4), ranges from 0.3 to 0.7, depending on  $W^2$  and  $Q^2$ . Considering these experimental conditions, for the numerical calculations, we will make use of the value  $\varepsilon \approx 0.5$  for whole ranges for  $W$  and  $Q^2$  for brevity.

Before going further, we want to examine the  $K^*$ -exchange in the  $t$  channel and  $\kappa_{\Lambda^*}$  effect in the  $u$ -channel. These contributions were turned out to be negligible in explaining the experimental data for the photoproduction off the proton target [9, 10]. In Figure 3, we plot the total cross sections for the electroproduction off the proton target without the  $D_{13}(2150)$  contribution. Here, the photon virtuality is taken to be the center value of the kinematic region  $(0.9 \sim 2.4)$  GeV<sup>2</sup> and the cutoff mass to be 620 MeV as a trial. We examine the various cases of  $g_{K^*N\Lambda^*}$  and  $\kappa_{\Lambda^*}$ :  $g_{K^*N\Lambda^*} = (0, \pm 1.5)$  and  $\kappa_{\Lambda^2} = (0, \kappa_n)$ . As shown in the figure, the effects of those contributions are negligible, showing a few percent changes from that without those contributions (solid), although there appears slight increasing in the higher  $W$  region with the finite  $\kappa_{\Lambda^*}$  value  $\sim \kappa_n$ . If we take the theoretical estimations from the SU(6) quark model [33, 37] and phenomenological study with the  $K^*$  Regge trajectory [38], we have  $g_{K^*N\Lambda^*} \approx 10$  and  $g_{K^*N\Lambda^*} = 7.1$  (or  $-12.6$ ), respectively. We verified that these estimations gives only small differences with about  $(5 \sim 10)\%$  in

| $g_{K\Lambda^*}$ | $ g_{K^*N\Lambda^*} $ | $ g_1 $                      | $h_1$ | $h_2$ | $g_{\gamma KK^*}$          | $\kappa_{\Lambda^*}$                  |
|------------------|-----------------------|------------------------------|-------|-------|----------------------------|---------------------------------------|
| 11               | 1.5                   | free parameter<br>(0 ~ 1.52) | -0.73 | 2.02  | $\frac{0.254}{\text{GeV}}$ | free parameter<br>( $\sim \kappa_n$ ) |

TABLE II: Electromagnetic and strong coupling constants of the present work.

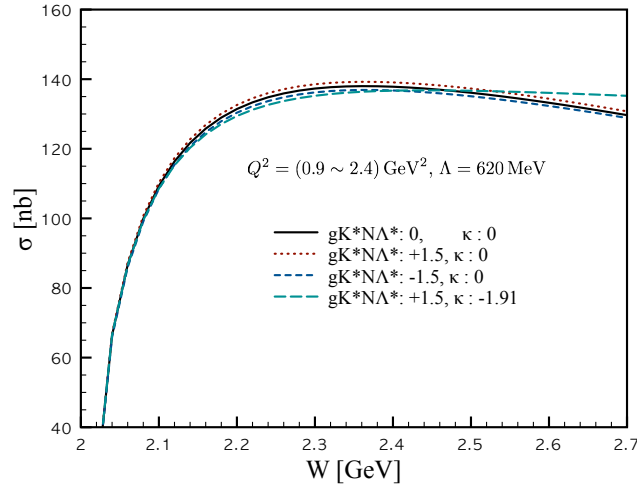


FIG. 3: Total cross section without the  $D_{13}(2150)$  contribution, varying the values of  $g_{K^*N\Lambda^*}$  and  $\kappa_{\Lambda^*}$ . Here, we choose the center value of  $Q^2 = (0.9 \sim 2.5) \text{ GeV}^2$  and the cutoff mass  $\Lambda = 620 \text{ MeV}$  in Eq. (15).

the cross section, comparing to that without the  $K^*$  exchange. Hence, taking into account that the tree-level Born approximation is well valid in the low energy region and the contact-term dominance, in addition to the  $K$  exchange, as supported theoretically and experimentally, we can rather safely ignore those  $K^*$  and  $\kappa_{\Lambda^*}$  contributions from the calculations hereafter, i.e.  $(g_{K^*N\Lambda^*}, \kappa_{\Lambda^*}) = 0$ .

Considering all the discussions and ingredients mentioned above, we are now ready to compute various physical quantities for the  $\Lambda^*$  electroproduction off the proton target. First, we show the numerical results for the differential cross section  $d\sigma/d\Omega$  as a function of  $\cos\theta$  in Figure 4 for the center value of the various photon virtuality intervals and  $W$  values. For instance, we choose  $Q^2 = 1.65 \text{ GeV}^2$  for the numerical calculations when the experimental data were accumulated for  $Q^2 = (0.9 \sim 2.4) \text{ GeV}^2$ . The experimental data are taken from Ref. [2]. The solid lines indicate the full calculation results with the  $D_{13}(2150)$  contribution, whereas the dash lines those without it. To reproduce the data qualitatively well, we determine  $|g_1| = 0.078$  with  $\phi_{\text{phase}} = 3\pi/2$  and the cutoff mass  $\Lambda = 620 \text{ MeV}$ , which is about 8% smaller than that for the photoproduction [7, 9, 10]. From the figure, one can see that the resonance contribution plays an important role to reproduce the data with considerably good agreement. As for  $W \lesssim 2.3 \text{ GeV}$ , the resonance contribution represents obvious improvements to the results, while the differences between the curves with and without it get diminished as  $W$  increases. As  $W$  goes beyond about  $2.4 \text{ GeV}$ , our theoretical model becomes hard to reproduce the data, although the theoretical curves still reproduce the data in the backward scattering regions  $\cos\theta \lesssim 0$ . Note that this sizable resonance contribution is quite different from the conclusion of Ref. [2], in which the nucleon resonance contributions are assumed to be inappreciable.

In the panel (A) of Figure 5, we present the numerical results for the total cross sections as functions of  $W$  with (solid) and without (dash) the  $D_{13}(2150)$  contribution for the whole  $K^+$  angle regions:  $-1 \leq \cos\theta \leq 1$ . We also show the resonance contribution separately by the long-dash line. The experimental data are taken from Ref. [2]. Again, we observe that the  $D_{13}(2150)$  plays a crucial role to reproduce the data in the vicinity of  $W = 2.2 \text{ GeV}$ . As noted in the differential cross sections shown in Figure 4, we can not reproduce the experimental data well beyond  $W \approx 2.5 \text{ GeV}$ . Moreover, by comparing the numerical results with the data near the threshold, there can be additional resonance contributions around  $W = 2.1 \text{ GeV}$ , since the theory underestimates the strength of the production in that region. Possible candidates can be  $N^*(2040, 3/2^+; *)$ ,  $N^*(2060, 5/2^-; **)$ , and  $N^*(2100, 1/2^+; *)$ , where  $*$  indicates the confirmation level [19], although we leave them for the future works, since we do not have much information relevant for the  $\Lambda^*$  electroproduction at this moment. In the panel (B) of Figure 5, we depict the total cross sections from the contact-term (solid) and  $K$ -exchange (dash) contributions separately for the whole polarization states averaged (thick) and the longitudinal one only (thin), since we verified that these two channels dominates the production process beside the resonance contribution. As understood by each curves, the longitudinal-polarization contribution effects much on the  $K$  exchange in the  $t$  channel, in comparison to the contact-term one as expected, i.e. the longitudinal component selects the  $K$  exchange. Numerically, about 70% of the total production rate is produced from the longitudinal polarization for the  $K$  exchange contribution, whereas only about 30% from it for the contact-term one. Note that this observation is quite different from the photoproduction case, in which the contact-term contribution almost dominates the production rate. This interesting tendency can be understood in

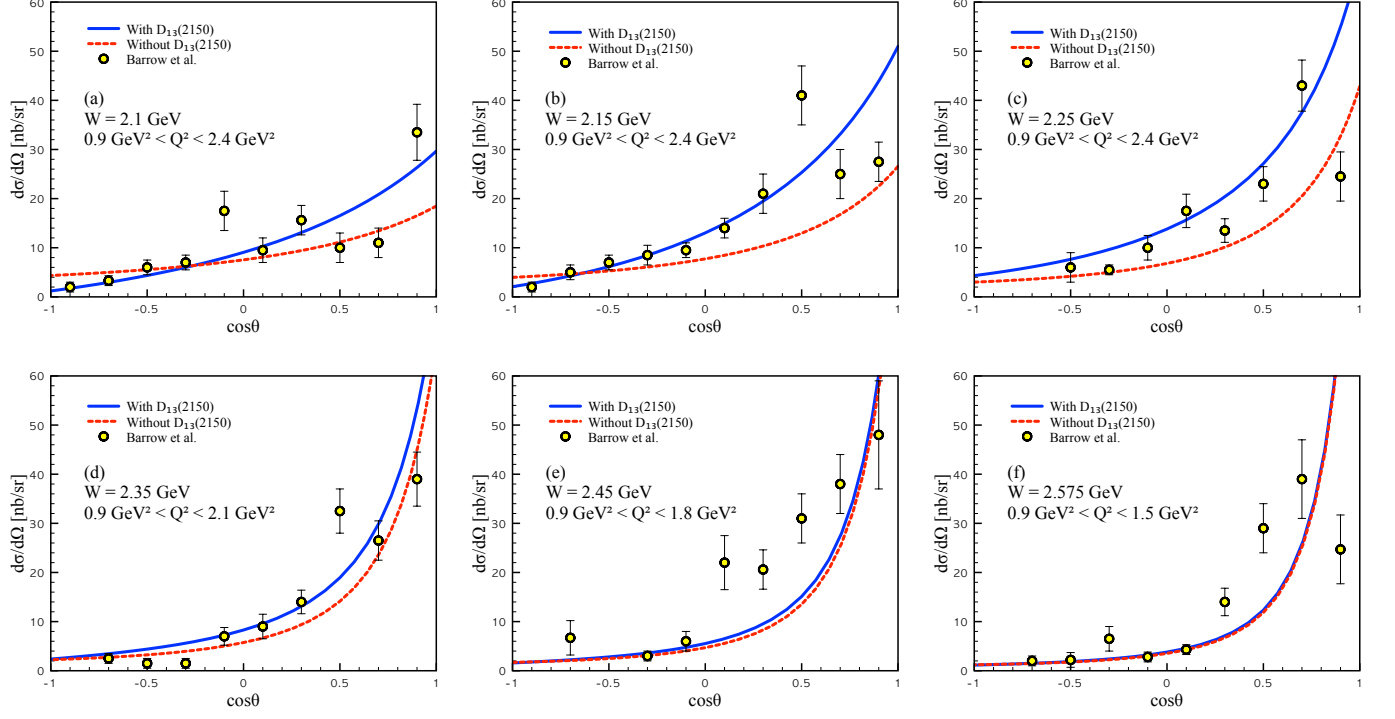


FIG. 4: Differential cross section  $d\sigma/d\Omega$  [ $\mu\text{b/sr}$ ] as functions of  $\cos\theta$  for different  $W$  values with (solid) and without (dash)  $D_{13}(2150)$  contribution. The curves are computed at the middle values of the  $Q^2$  intervals, shown in each panel. Here, we have chosen  $\Lambda = 620$  MeV and  $\varepsilon \approx 0.5$ . Experimental data are taken from Ref. [2].

detail by the following: In our kinematical setup,  $k_3 \cdot \epsilon$  in the  $K$  exchange in the  $t$  channel in Eq. (13) can be written by

$$k_3 \cdot \epsilon_x = k_3 \sin\theta, \quad k_3 \cdot \epsilon_y = 0, \quad k_3 \cdot \epsilon_z = \frac{\sqrt{2\varepsilon}}{Q} [k_1 E_3 - k_3 E_1 \cos\theta], \quad (17)$$

where  $k_{1,3}$  denote the three momenta for  $k_{1,3}$ . Note that the last term,  $k_3 \cdot \epsilon_z$  only exists for the electroproduction case and enhances the production rate by  $(k_3 \cdot \epsilon_z)^2$  in comparison to the photoproduction. On the contrary, the contact term, which contains  $(\epsilon_{\Lambda^*} \cdot \epsilon)$ , in which  $\epsilon_{\Lambda^*}$  stands for the vector part of the Rarita-Schwinger field, is not much affected by the longitudinal component of the virtual photon. These differences between the two dominant contributions for the electroproduction indicate that the  $\phi$  distribution in the GJ frame can be different from that of the photoproduction, in which the spin-3/2 states of  $\Lambda^*$  decay into  $K^- p$  mainly via the contact-term contribution. We will examine this difference in detail below soon. In the panel (C) of Figure 5, we also draw the numerical results for the total cross section in the same manner with the panel (A) for the limited  $\theta$ -angle region, i.e.  $\cos\theta \leq 0.6$ , comparing with the experimental data [2]. In the presence of the  $D_{13}(2150)$  contribution, we can reproduce the experimental data qualitatively well, while the production rate for the region  $W = (1.95 \sim 2.2)$  is still underestimated. In the panel (D) of Figure 5, we depict the numerical results for the total cross sections as functions of  $Q^2$  for  $W = (2.22 \sim 2.43)$  GeV, being represented by the shade area. Experimental data and the parameterized curve (dot) are taken from Ref. [2]. The parameterization was done by  $\sigma \propto (m_{\text{para}}^2 + Q^2)^{-2}$  with  $m_{\text{para}}^2 = 2.73 \text{ GeV}^2$ . We observe that the experimental data are well included within the theoretically calculated area (shaded).

From now on, we want to discuss the  $\phi$  distribution in the GJ frame as discussed in several literatures [1, 3, 10]. Considering the  $\Lambda^*$ -rest frame, one can construct a kinematic frame with the colliding meson and target nucleon, producing  $\Lambda^*$  at rest, then it decays into  $K^-$  and  $p$ , i.e. the GJ frame. Interestingly, the angular distribution of  $K^-$  can be fully derived from the simple spin statistics of the system [1]. The  $\phi$  distribution can be simply written as follows:

$$\mathcal{F}_{K^-}(\phi) \approx [A \sin^2 \phi]_{S_{\Lambda^*}=3/2} + \left[ B \left( \frac{1}{3} + \cos^2 \phi \right) \right]_{S_{\Lambda^*}=1/2}, \quad (18)$$

where  $\phi$  denotes the decaying angle of  $K^-$  in the  $\Lambda^*$  rest frame. If the  $K^-$  decays from  $\Lambda^*(S = 3/2)$ , the distributions



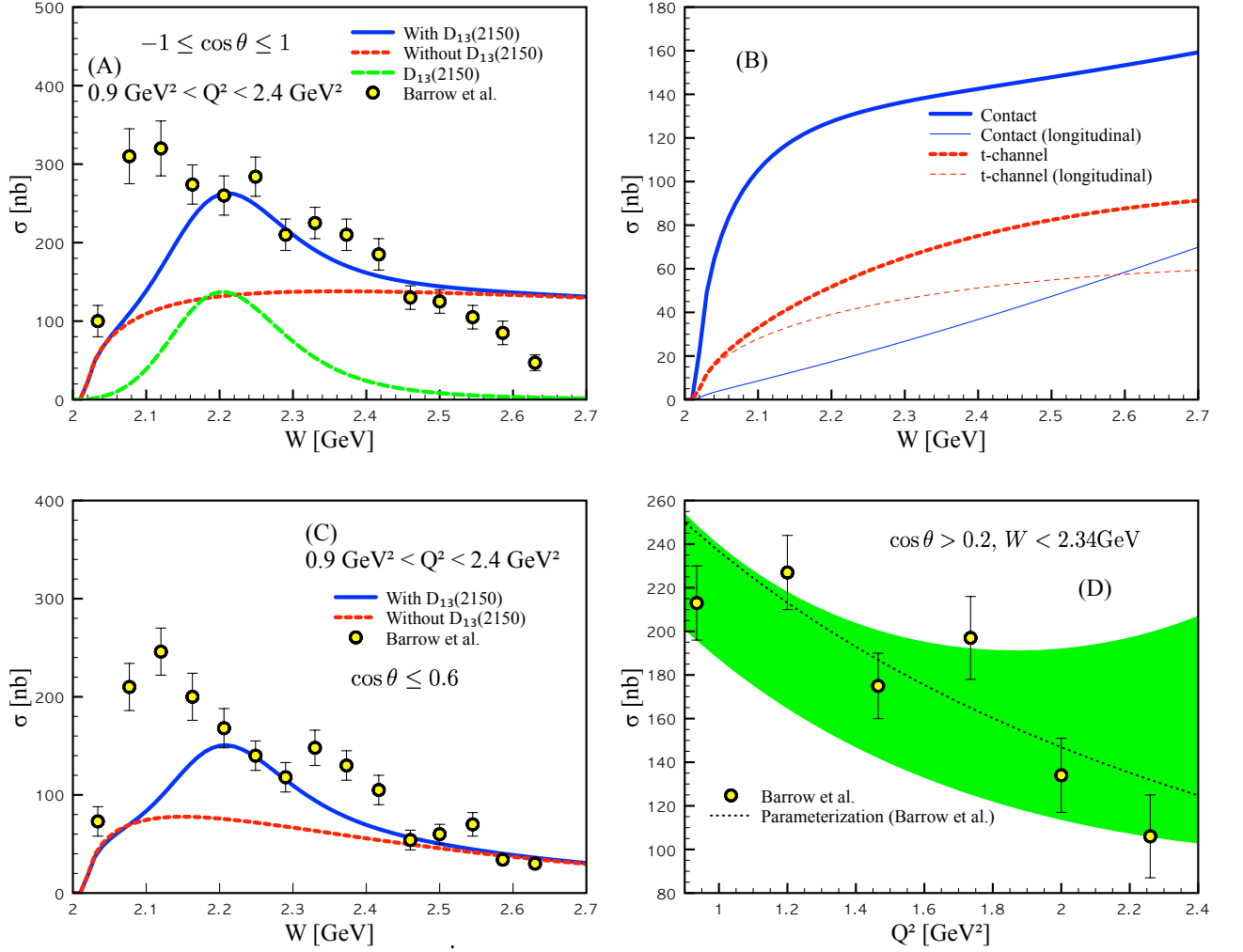


FIG. 5: (A) Total cross sections for  $-1 \leq \cos \theta \leq 1$  as functions of  $W$  with  $Q^2 = 1.65 \text{ GeV}^2$ . The solid and dash line denote those with and without the  $D_{13}(2150)$  contribution, respectively. (B) Total cross sections from the contact-term and  $t$ -channel  $K$ -exchange contributions for the transverse and longitudinal photons, separately. (C) Total cross sections  $\cos \theta \leq 0.6$  as functions of  $W$  with  $Q^2 = 1.65 \text{ GeV}^2$  in the same manner with (A). (D) Total cross section as a functions of  $Q^2$  for  $\cos \theta > 0.2$  and  $W = (2.22 \sim 2.43) \text{ GeV}$ , given by the shaded area. The dot line stands for the parameterized curve by  $\sigma \propto (m_{\text{para}}^2 + Q^2)^{-2}$  with  $m_{\text{para}}^2 = 2.73 \text{ GeV}^2$  [2]. All the experimental data are taken from Ref. [2]

follows the first term in the right-hand-side of Eq. (18). On the contrary, if it is does from  $\Lambda^*(S = 1/2)$  state, it can be described by the second term. Here,  $A$  and  $B$  are real values and stand for the relative strength for each spin states, satisfying the normalization  $A + B \approx 1$ . In Ref. [2], the authors included an additional term  $C \cos \phi$ , indicating the interferences with the backgrounds, although we omit it for simplicity here. Theoretically, the strength factors  $A$  and  $B$  can be estimated and computed by the following parameterization, remembering that the final-state  $\Lambda^*$  spins are just summed,

$$A = \frac{d\sigma_{\Lambda^*(S=3/2)}}{d\sigma_{\text{total}}}, \quad B = \frac{d\sigma_{\Lambda^*(S=1/2)}}{d\sigma_{\text{total}}}, \quad (19)$$

satisfying the normalization condition [10]. We also define the ratio of the coefficients for further purpose by

$$\mathcal{R} = \frac{A}{B}. \quad (20)$$

If  $\mathcal{R}$  is (larger, smaller) than unity, the  $\Lambda^*(S = 3/2, 1/2)$  decay will dominates the process. If one draws the curves of the  $\phi$  distributions in Eq. (18) for  $\Lambda^*(S = 3/2)$ , the curve shape becomes a hill ( $\frown$ ), whereas a valley ( $\smile$ ) for

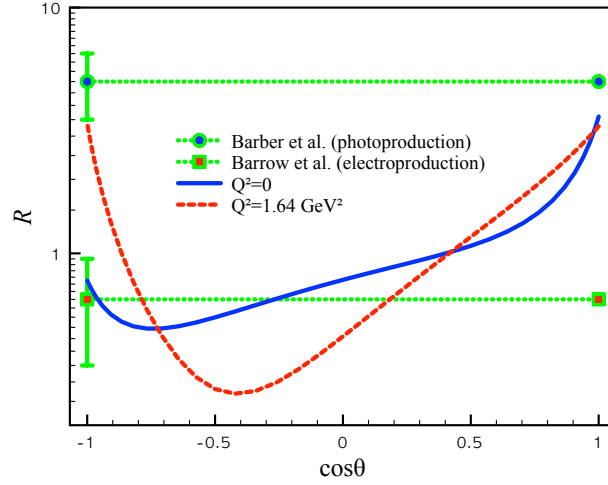


FIG. 6: Ratio for the  $\Lambda(1520)$  spin-state distribution,  $\mathcal{R}$  in Eq. (20) as functions of  $\cos\theta$  for  $Q^2 = 0$  (solid) and  $1.64 \text{ GeV}^2$  (dash). Experimental data are taken from the LAMP2 [1] (circle) and CLAS [2] (square) collaborations.

$\Lambda^*(S = 1/2)$ , as functions of  $\cos\phi$ . For convenience, we assign the first by *A-type* and the second by *B-type*, considering their coefficients named. In Figure 6, we draw the ratio  $\mathcal{R}$  in Eq. (20) as functions of  $\cos\theta$  for  $Q^2 = 0$  (solid), i.e. photoproduction, and  $Q^2 = 1.64 \text{ GeV}^2$  representing the (almost) average value for the CLAS experiment [2]. The horizontal dot lines stand for the experimental data taken from the LAMP2 (Barber *et al.*) [1] (circle) and CLAS (Barrow *et al.*) (square) [2], with the errors. For the region of  $\cos\theta \gtrsim 0.5$ , i.e. the forward  $K^+$  scattering region, the photoproduction is dominated by  $\Lambda^*(S = 3/2)$  ( $\mathcal{R} > 1$ ). Similar tendency is observed also for the electroproduction. Approaching to the backward  $K^+$  scattering region,  $\Lambda^*(S = 1/2)$  becomes getting over  $\Lambda^*(S = 3/2)$  for the both EM productions. However, the strength of  $\Lambda^*(S = 1/2)$  is much stronger for the electroproduction than that for the photoproduction, due to the  $K$ -exchange enhancement in the electroproduction as discussed above. At very backward scattering region  $\cos\theta \approx -1$ ,  $\Lambda^*(S = 3/2)$  increases for the electroproduction, while the photoproduction is still dominated  $\Lambda^*(S = 1/2)$ . Comparing the experimental data with our theoretical estimations, the LAMP2 data can correspond to the very forward region  $\cos\theta \approx 1$ . The CLAS data can indicate the region  $\cos\theta \lesssim 0.4$ , saying, roughly the backward scattering region.

In Figure 7, we plot the  $\phi$  distribution in Eq. (18) as functions of  $\cos\phi$  and  $\cos\theta$  at  $W = 2.22 \text{ GeV}$ , which is a center value for  $W = (1.95 \sim 2.43) \text{ GeV}$ , for  $Q^2 = 1.05 \text{ GeV}^2$  (A),  $1.35 \text{ GeV}^2$  (B),  $1.65 \text{ GeV}^2$  (C), and  $2.10 \text{ GeV}^2$  (D). Note that there appear little difference observed from the different photon virtuality. As for the electroproduction, except for the very forward and backward scattering regions of  $K^+$ ,  $\cos\theta \approx \pm 1$ , the  $\phi$  distribution are dominated by the B-type curves as functions of  $\cos\phi$ , signaling the dominant  $\Lambda^*(S = 1/2)$  cotribution, being strengthened by the  $K$ -exchange contribution in the  $t$  channel. We also observe the clearly different A-type curves for almost all the  $\theta$  regions for the photoproduction in the panel (E), in comparison to those for the electroproduction:  $\Lambda^*(S = 3/2)$  dominates the production process, due to the contact-term contribution.

In the panel (A) of Figure 8, we draw the  $\phi$  distribution for a typical  $K^+$  angle,  $\theta = 30^\circ$ , which manifests the difference between the two EM productions. Here, we choose  $W = 2.43 \text{ GeV}$  and  $Q^2 = 1.05 \text{ GeV}^2$ . The experimental data for the electroproduction are taken from Ref. [2]. Although the data are quite scattered so that it is difficult to have a decisive conclusion, the difference between the photo (A-type) and electroproduction (B-type) curves are quite obvious from the theoretical results. In Figure 9, we draw the numerical results for the  $t$ -momentum transfer distribution for various intervals  $W = (2.02 \sim 2.21) \text{ GeV}$  (A),  $(2.21 \sim 2.43) \text{ GeV}$  (B), and  $(2.43 \sim 2.65) \text{ GeV}$  (C) for  $Q^2 = 1.65 \text{ GeV}^2$ . The experimental data for  $Q^2 = (0.9 \sim 2.4) \text{ GeV}^2$  are again taken from Ref. [2]. The thick solid and dash lines indicate the different  $W$  values. The thin solid lines denote the parameterized one via  $d\sigma/dt \propto e^{bt}$ , where  $b$  stand for  $2.3 \pm 0.1$  (A),  $2.4 \pm 0.2$  (B), and  $1.8 \pm 0.2$  (C) [2]. Although we are looking at only a single  $Q^2$  value for the numerical calculations, the numerical results reproduce the data qualitatively.

We now discuss the  $\Lambda^*$  photoproduction with the  $D_{13}(2150)$  contribution, whose strong coupling and phase factor have been determined for reproducing the electroproduction as above. In the panel (A) of Figure 10, we show the numerical results for it off the proton target as functions of  $E_\gamma$  with (solid) and without (dash) the resonance contribution. The experimental data are taken from Figure 3 of Ref. [5]. The circle, star, and square denote the data from LAMP2 [1], eg3-run of CLAS [5], and g11-run of CLAS [36], respectively. We observe that the resonance

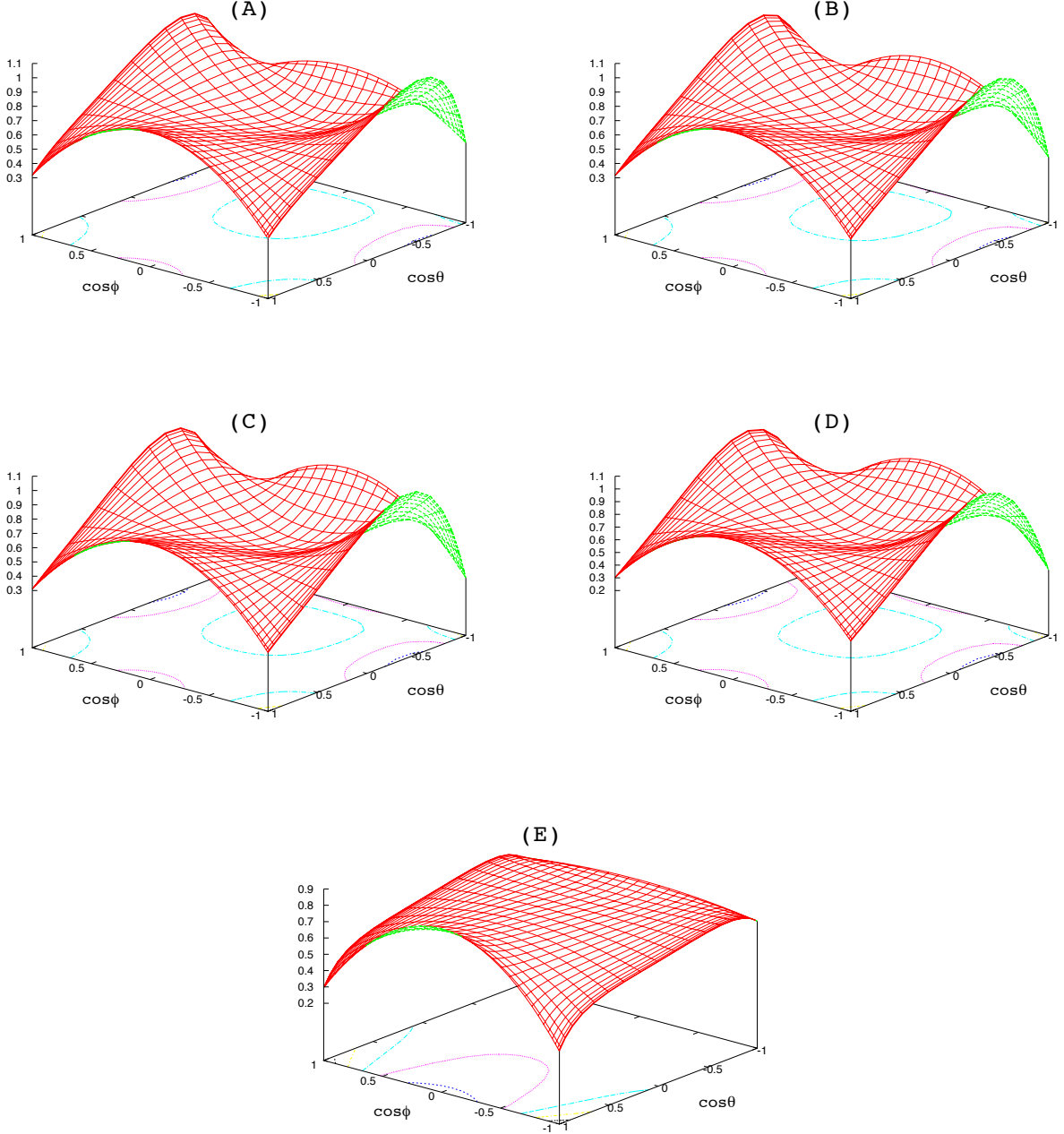


FIG. 7:  $K^-$  decay angle ( $\phi$ ) distribution in Eq. (18) as functions of  $\cos \phi$  and  $\cos \theta$  at  $W = 2.22$  GeV, which is a center value for  $W = (1.95 \sim 2.43)$  GeV, for  $Q^2 = 1.05 \text{ GeV}^2$  (A),  $1.35 \text{ GeV}^2$  (B),  $1.65 \text{ GeV}^2$  (C), and  $2.10 \text{ GeV}^2$  (D). In panel (E), we plot the same for the photoproduction, i.e.  $Q^2 = 0$ . For all the cases, we included the  $D_{13}(2150)$  contribution.

contribution does not make drastic changes in comparison to that shown in the electroproduction in the panel (A) of Figure 5. There appears only about 10% increasing of the peak around  $E_\gamma \approx 2$  GeV, due to the resonance. We also observe that the numerical results with the  $D_{13}(2150)$  contribution reproduce those experimental data qualitatively well as shown in the panel (A) of Figure 10, although the data point of eg3-run of CLAS [5] at  $(\sigma, E_\gamma) \approx (1.4 \text{ nb}, 2 \text{ GeV})$  can not be explained even with the resonance. The differential cross sections for the photoproduction are also given as functions of  $\cos \theta$  for  $E_\gamma \approx 2.15$  GeV in the panel (B) of Figure 10 in the same manner with the panel (A). The experimental data are taken from Ref. [3] for various meson-meson and meson-baryon channels, using the sideband

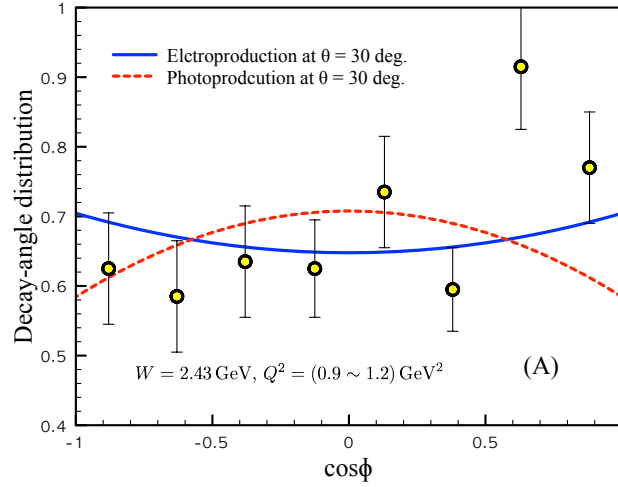


FIG. 8: Total cross sections as functions of  $Q^2$  with (solid) and without (dash)  $D_{13}(2150)$  contribution. For the theoretical calculation, we choose  $W = 2.43$  GeV only. The experimental data are taken from Ref. [2].

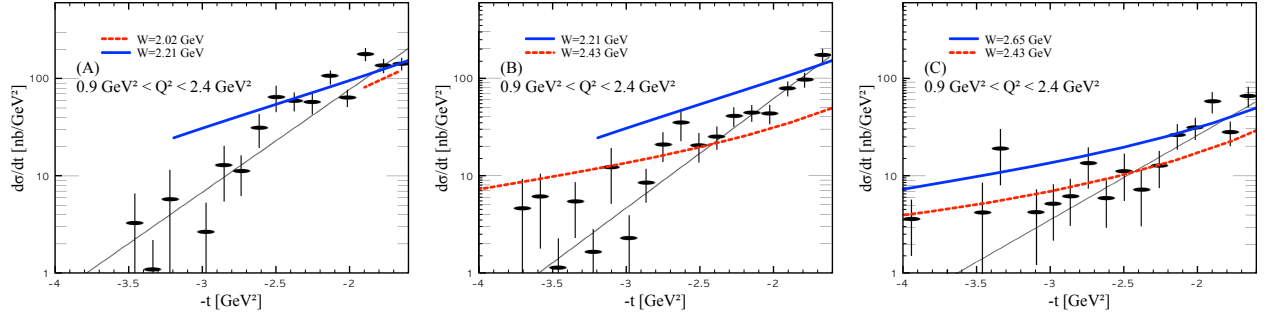


FIG. 9:  $t$ -momentum transfer distribution,  $d\sigma/dt$  as functions of  $-t$  for  $W = (2.02 \sim 2.21)$  GeV (A),  $(2.21 \sim 2.43)$  GeV (B), and  $(2.43 \sim 2.65)$  GeV (C). The solid and dash lines indicate each  $W$  values. Here, we choose  $Q^2 = 1.65$  GeV<sup>2</sup> for the theoretical calculations for brevity. Experimental data are taken from Ref. [2] and are parameterized by  $e^{bt}$  given in the thin solid lines in each panel with  $2.3 \pm 0.1$  (A),  $2.4 \pm 0.2$  (B), and  $1.8 \pm 0.2$  (C).

(SB) and Monte-Carlo (MC) methods. There appears considerable enhancement in the forward scattering region due to the resonance by about 20%, whereas one sees slight decreasing of the production rate in the backward scattering region, although the overall shapes of the curves are comparable to the experimental data.

All the strong couplings, having determined for  $\gamma^*p \rightarrow K^+\Lambda^*$  as above, can be directly used for the neutron-target case, whereas the EM couplings should be changed. Especially, we focus on the magnetic transition coupling  $h_{1,2}$ . Because there has not been experimental and theoretical information on the helicity amplitudes for neutral  $D_{13}(2150)$ , i.e.  $A_{1/2,3/2}^{n^*(2150) \rightarrow \gamma n}$ , not like the positive one [19, 34], we try to make a rough estimation for them, employing the information for  $D_{13}(2080)$ , since it was considered to be  $D_{13}(2150)$  [19, 34] and may reflect the EM properties of  $D_{13}(2150)$  partially. Employing the experimental data [32], we can write the following relation:

$$A_{1/2,3/2}^{n^*(2150) \rightarrow \gamma n} \approx -\mathcal{R}_{A_{1/2,3/2}} A_{1/2,3/2}^{p^*(2150) \rightarrow \gamma n} = -\left| \frac{A_{1/2,3/2}^{n^*(2080) \rightarrow \gamma n}}{A_{1/2,3/2}^{p^*(2080) \rightarrow \gamma p}} \right| A_{1/2,3/2}^{p^*(2150) \rightarrow \gamma n}. \quad (21)$$

Note that we multiplied the negative sign for the neutral helicity amplitudes. Making use of the above equation, we obtain

$$h_1^{n^*} = -4.32, \quad h_2^{n^*} = 1.72. \quad (22)$$

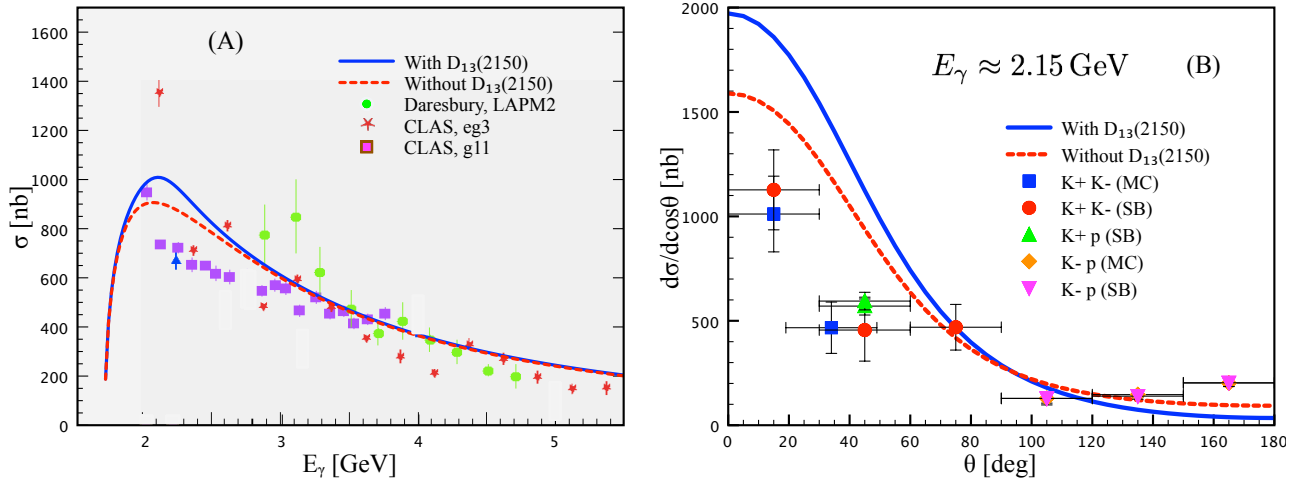


FIG. 10: (A) Total cross section for the *photoproduction* of  $\Lambda(1520)$  ( $Q^2 = 0$  and  $\varepsilon = 0$ ) off the proton target with (solid and dot) and without (dash)  $D_{13}(2150)$  contribution, which is represented by the long-dash line. The experimental data are duplicated from Figure 3 in Ref. [5]. The circle, star, and square denote the data from Refs. [1], [5], and [36], respectively. (B) The differential cross sections for the photoproduction are also given as functions of  $\cos\theta$  in the same manner with the panel (A). The experimental data are taken from Ref. [3] with various particle measurement channels using the sideband (SB) and Monte-Carlo (MC) methods.

In the panel (A) of Figure 11, we depict the differential cross sections for the  $\gamma^*n \rightarrow K^0\Lambda^*$  as functions of  $\cos\theta$  for different  $W$  values, using Eq. (22). The  $Q^2$  intervals are the same with those for each  $W$ , given in Figure 4. We again set  $(g_{K^*\Lambda\Lambda^*}, \kappa_{\Lambda^*}) = 0$  for simplicity, since we verified that those contributions are almost negligible similar to the proton-target case. If this is the case, the neutron-target production rate is generated almost by the nucleon resonance and  $s$ -channel magnetic contribution proportional to  $\kappa_n$ . From the panel (A), it can be understood that the production rate is almost dominated by the  $D_{13}(2150)$  contribution, and the region beyond  $W \approx 2.35$ , in which the resonance effects are diminished, the differential cross sections becomes almost flat due to the  $s$ -channel nucleon-pole contribution. The total cross sections for the electroproduction off the neutron target as functions of  $W$  are given in the panel (B) of Figure 11 up to  $W = 2.4$  GeV. As observed, the  $D_{13}(2150)$  contribution (solid) produces almost all the strength for the total cross section, showing a peak at  $W \approx M_R$ , while the other is done by the  $s$ -channel nucleon-pole contribution. Now we introduce a quantity, *averaged total cross section*, which is defined by

$$\bar{\sigma} = \frac{1}{|W_{\max} - W_{\min}|} \int_{W_{\min}}^{W_{\max}} \sigma(W) dW. \quad (23)$$

Employing Eq. (23), we compute the ratio of the total cross section for the electroproduction off the proton and neutron targets with the  $D_{13}(2150)$  contribution, resulting in

$$\mathcal{R}_{p/n}^{\gamma^*} \equiv \frac{\bar{\sigma}_{\gamma^*p \rightarrow K^+\Lambda^*}}{\bar{\sigma}_{\gamma^*n \rightarrow K^0\Lambda^*}} \approx \frac{167.36 \text{ nb}}{104.34 \text{ nb}} = 1.60, \quad (24)$$

where we choose  $W_{(\min, \max)} = (\text{threshold}, 2.7)$  GeV at  $Q^2 = 1.65 \text{ GeV}^2$ . From the same theoretical calculation with Eq. (24), we obtain the following value for the photoproduction of  $\Lambda^*$ ,

$$\mathcal{R}_{p/n}^{\gamma} \equiv \frac{\bar{\sigma}_{\gamma p \rightarrow K^+\Lambda^*}}{\bar{\sigma}_{\gamma n \rightarrow K^0\Lambda^*}} \approx \frac{758.71 \text{ nb}}{40.68 \text{ nb}} = 18.65, \quad (25)$$

which is about ten-times larger than that for the electroproduction. Hence, we can conclude that the contact-term dominance is still valid for the photoproduction case as far as we work with the present theoretical framework, in comparison to the electroproduction. It is worth mentioning that, from the CLAS eg3-run data [5], the photoproduction of  $\Lambda^*$  off the neutron target was estimated to be comparable with that for the proton target case. Although the maximum value of the total cross section shown in Figure 11 looks comparable to the eg3-run data, the curve shape of the eg3-run neutron data can not be reproduced by our simple single-resonance ( $D_{13}$ ) calculations on top of the negligible  $K^*$  contribution. Hence, we can expect that the curve shape of the eg3-run neutron data, which is

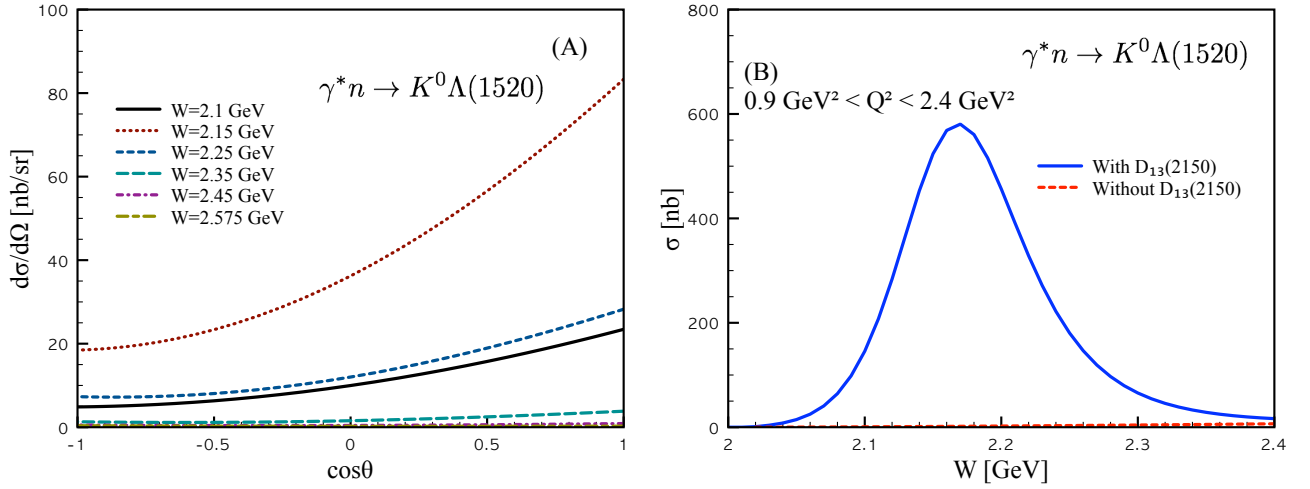


FIG. 11: (A) Differential cross sections for the  $\gamma^*n \rightarrow K^0\Lambda^*$  as functions of  $\cos\theta$  for different  $W$  values. The  $Q^2$  intervals are the same with those given in Figure 4. (B) Total cross sections for the  $\gamma^*n \rightarrow K^0\Lambda^*$  as functions of  $W$  for  $Q^2 = 1.65 \text{ GeV}^2$  with (solid) and without (dash) the  $D_{13}(2150)$  contribution.

similar or slightly smaller than that for the proton target data [5], are made of the combination of the many nucleon resonances with very small Born-term background. In other words, the  $\Lambda^*$  EM productions off the neutron target is a very useful tool to investigate the resonances contributions, since the background is considerably tiny only with the possibly small  $K^*$ -exchange contribution.

#### IV. SUMMARY AND OUTLOOK

In the present work, we have studied the electroproduction of  $\Lambda^*$  off the nucleon target  $\gamma^*p \rightarrow K^+\Lambda^*$ , employing the tree-level Born approximation. Taking into account the results in our previous work [7, 9, 10], we constructed an effective theoretical framework for the present purpose. We computed theoretically total and differential cross sections,  $\phi$  distribution in the GJ frame, ratio for the  $\Lambda^*$  spin states, and  $t$ -momentum transfer distributions. All the relevant model parameters were determined using the presently available experimental and theoretical information. Below, we list important observations in the present work:

- The angular and energy dependences for the cross sections for the proton target are reproduced qualitatively well and exhibits the crucial effects from the  $D_{13}(2150)$  resonance in the vicinity of  $W \approx 2.1$  GeV. In order to reproduce the data, we determine  $g_{KN^*\Lambda^*}$  to be  $7.8 \times 10^{-2}$ , which is smaller than those obtained from the SU(6) quark-model estimations for  $D_{13}(2080)$ , with the phase factor  $e^{3i\pi/2}$ . The resonance enhances the production rate in the forward-scattering region in general, on top of the contact-term and  $K$ -exchange Born contributions.
- The longitudinal component ( $S_z = 0$ ) of the virtual photon selects the kaon-exchange contribution in the electroproduction of  $\Lambda^*$ , being different from the photoproduction case. This selection makes  $\Lambda^*(S = 1/2)$  increased, being comparable to  $\Lambda^*(S = 3/2)$ , resulting in the different structures of the  $\phi$  distribution, as observed in the CLAS electroproduction experiment. We confirm this difference by computing the  $\phi$  distribution as functions of  $\theta$  and  $\phi$  for the electro and photoproductions, separately. From the numerical results, we have the following tendency for the  $\Lambda^*$  EM productions off the proton target approximately:

$$\gamma p \rightarrow K^+\Lambda^*: \sigma_{\text{contact}} \gg \sigma_K \quad \text{and} \quad \gamma^* p \rightarrow K^+\Lambda^*: \sigma_{\text{contact}} \approx 2\sigma_K$$

- As for the  $\Lambda^*$  photoproduction off the proton-target case, the effect from  $D_{13}(2150)$  is considerably small in comparison to that shown for the electroproduction, since the contact term dominates the production rate for the photoproduction. Calculated total cross section for the  $\Lambda^*$  photoproduction with the resonance is comparable qualitatively with LAMP2 and g11-run data of CLAS, whereas the eg3-run data of CLAS exceeds much from our result around  $E_\gamma = 2$  GeV. Again, the resonance effects appear to enhance the forward-scattering production rate.

- In contrast, the  $\Lambda^*$  electroproduction off the neutron target is saturated by the nucleon resonance contributions, such as  $D_{13}(2150)$  in the absence of the contact-term and  $K$ -exchange contributions, due to the electric-charge conservation, as far as the  $K^*$ -exchange contribution in the  $t$  channel is taken into account to be negligible. From this observation, the  $\Lambda^*$  EM production off the neutron target can be considered as one of the best production channels to explore the nucleon-resonance spectra, accompanying with considerably small backgrounds.
- The contact-term dominance, which is one of the key ingredients to understand the  $\Lambda^*$  EM production off the proton target, becomes weak for the electroproduction case according to the considerable resonance effects as well as the enhanced  $K$ -exchange contribution, although its strength is still sizable in terms of the production rate. This tendency can be also shown alternatively from the ratio of the cross sections off the proton and neutron targets, being averaged from the threshold to  $W = 2.7$  GeV, with a single resonance contribution from  $D_{13}(2150)$ :

$$\mathcal{R}_{p/n}^{\gamma^*} \approx 1.60 \quad \text{and} \quad \mathcal{R}_{p/n}^{\gamma} \approx 18.65$$

As for the next steps to scrutinize the  $\Lambda^*$  EM productions, 1) one needs to consider more resonance contributions near the threshold region especially for the neutron target case and 2) make clearer the effects from other high-spin strange mesons, including  $K^*$ . Using the present work as a starting point, 3) it is necessary to compute more meaningful physical observables, which manifest the typical production mechanisms of the  $\Lambda^*$  EM productions and play the role of useful guides for the future experiments. As for addressing 1), we plan to employ the isobar model [39] for the  $\Lambda^*$  EM productions to include the resonance contributions systematically and to reproduce the neutron data realistically, while the  $t$ -channel Regge trajectories can be also applied to address 2), taking into account the higher-spin strange meson contributions simultaneously. The Feynman-Regge interpolation prescription, suggested in Ref. [10], can be also employed to extend the present results to higher energy regions in a consistent manner. This extension to the higher energy will be useful, considering the planned future upgrade of the beam energy in CLAS of Jefferson laboratory, i.e. CLAS12 at Hall B [40]. As for 3), we may compute polarization observables, such as the beam, target, and recoil  $\Lambda^*$  polarizations, in addition to the double-polarization ones. Related and combined works are under progress and will appear elsewhere in the near future.

#### acknowledgment

The author is grateful to A. Hosaka, C. W. Kao, and S. H. Kim for fruitful discussions for the present work.

#### Appendix

Here we discuss about the photon polarization vectors and the definition of the polarization parameter  $\varepsilon$ . The photon polarization vectors in the present work are defined as follows:

$$\epsilon_x = (0, \sqrt{1+\varepsilon}, 0, 0), \quad \epsilon_y = (0, 0, \sqrt{1-\varepsilon}, 0, 0), \quad \epsilon_z = \sqrt{2\varepsilon} \left( \frac{k}{Q}, 0, 0, \frac{E_{\gamma^*}}{Q} \right). \quad (26)$$

and their norms squared are given by

$$\epsilon_x^2 = 1 + \varepsilon, \quad \epsilon_y^2 = 1 - \varepsilon, \quad \epsilon_z^2 = 2\varepsilon \left( \frac{k^2 - E_{\gamma^*}^2}{Q^2} \right) = 2\varepsilon, \quad (27)$$

where we have used  $k^2 = E_{\gamma^*}^2 + Q^2$  for the virtual photon. According to the gauge-invariance argument as in Ref. [26], the scattering amplitude can be simplified by omitting the scalar components. This simplification can be realized by setting all the 0-th components of the photon polarization vectors in Eq. (26) to be zero:

$$\epsilon'_x = (0, \sqrt{1+\varepsilon}, 0, 0), \quad \epsilon'_y = (0, 0, \sqrt{1-\varepsilon}, 0, 0), \quad \epsilon'_z = \sqrt{2\varepsilon} \left( 0, 0, 0, \eta \frac{E_{\gamma^*}}{Q} \right). \quad (28)$$

Note that we multiply the 4-th component of  $\epsilon'_z$  by  $\eta$ , which compensates the above simplification. Even with this change, the norm of the polarization vector should not be altered, and this consideration gives the value for  $\eta$ :

$$\epsilon_z'^2 = \epsilon_z^2 \rightarrow -2\varepsilon\eta \frac{E_{\gamma^*}^2}{Q^2} = 2\varepsilon \rightarrow \eta = -\frac{Q^2}{E_{\gamma^*}^2}. \quad (29)$$

This multiplication factor  $\eta$  is just the same with that given in Ref. [26], i.e.  $k^2/K_0^2$  in their notation. In literatures, which use the above simplification, motivated by the gauge invariance, an alternative definition  $\varepsilon_L \equiv |\eta|\varepsilon$  is frequently employed for the polarization three vector  $\epsilon_z = -\sqrt{2}\varepsilon_L(0, 0, E_{\gamma^*}/Q)$ . Note that we have an additional minus sign for the polarization three vector as already argued in Ref. [26].

- 
- [1] D. P. Barber *et al.*, Z. Phys. C **7**, 17 (1980).
  - [2] S. P. Barrow *et al.* [Clas Collaboration], Phys. Rev. C **64**, 044601 (2001).
  - [3] N. Muramatsu *et al.*, Phys. Rev. Lett. **103**, 012001 (2009).
  - [4] H. Kohri *et al.* [LEPS Collaboration], Phys. Rev. Lett. **104**, 172001 (2010).
  - [5] Z. W. Zhao *et al.* [CLAS Collaboration], AIP Conf. Proc. **1257**, 562 (2010).
  - [6] M. Nanova *et al.* [CBELSA/TAPS Collaboration], Eur. Phys. J. A **35**, 333 (2008).
  - [7] S. i. Nam, A. Hosaka and H. C. Kim, Phys. Rev. D **71**, 114012 (2005).
  - [8] H. Toki, C. Garcia-Recio and J. Nieves, Phys. Rev. D **77**, 034001 (2008).
  - [9] S. i. Nam, Phys. Rev. C **81**, 015201 (2010).
  - [10] S. i. Nam and C. W. Kao, Phys. Rev. C **81**, 055206 (2010).
  - [11] J. J. Xie and J. Nieves, Phys. Rev. C **82**, 045205 (2010).
  - [12] J. He and X. R. Chen, Phys. Rev. C **86**, 035204 (2012).
  - [13] K. S. Choi, S. i. Nam, A. Hosaka and H. C. Kim, J. Phys. G **36**, 015008 (2009).
  - [14] S. i. Nam and B. G. Yu, Phys. Rev. C **84**, 025203 (2011).
  - [15] S. Janssen, J. Ryckebusch, D. Debruyne and T. Van Cauteren, Phys. Rev. C **65**, 015201 (2002).
  - [16] Y. Oh and H. Kim, Phys. Rev. C **73**, 065202 (2006).
  - [17] S. H. Kim, S. i. Nam, Y. Oh and H. C. Kim, Phys. Rev. D **84**, 114023 (2011).
  - [18] S. H. Kim, S. i. Nam, A. Hosaka and H. C. Kim, arXiv:1211.6285 [hep-ph].
  - [19] J. Beringer *et al.* [Particle Data Group Collaboration], Phys. Rev. D **86**, 010001 (2012).
  - [20] W. Rarita and J. Schwinger, Phys. Rev. **60**, 61 (1941).
  - [21] L. M. Nath, B. Etemadi and J. D. Kimel, Phys. Rev. D **3**, 2153 (1971).
  - [22] H. Habermehl, C. Bennhold, T. Mart and T. Feuster, Phys. Rev. C **58**, 40 (1998).
  - [23] R. M. Davidson and R. Workman, Phys. Rev. C **63**, 025210 (2001).
  - [24] H. Habermehl, K. Nakayama and S. Krewald, Phys. Rev. C **74**, 045202 (2006).
  - [25] T. Mart, Phys. Rev. C **82**, 025209 (2010).
  - [26] C. W. Akerlof *et al.*, Phys. Rev. **163**, 1482 (1967).
  - [27] C. N. Brown *et al.*, Phys. Rev. D **8**, 92 (1973).
  - [28] T. Azemoon *et al.*, Nucl. Phys. B **95**, 77 (1975).
  - [29] E. Amaldi, S. Fubini and G. Furlan, Springer Tracts Mod. Phys. **83**, 1 (1979).
  - [30] R. A. Williams, C. R. Ji and S. R. Cotanch, Phys. Rev. C **46**, 1617 (1992).
  - [31] W. T. Chiang, S. N. Yang, L. Tiator and D. Drechsel, Nucl. Phys. A **700**, 429 (2002).
  - [32] C. Amsler *et al.* [Particle Data Group Collaboration], Phys. Lett. B **667**, 1 (2008).
  - [33] T. Hyodo, S. Sarkar, A. Hosaka and E. Oset, Phys. Rev. C **73**, 035209 (2006) [Erratum-ibid. C **75**, 029901 (2007)].
  - [34] A. V. Anisovich *et al.*, Eur. Phys. J. A **48**, 15 (2012).
  - [35] S. Capstick and W. Roberts, Phys. Rev. D **58**, 074011 (1998).
  - [36] The unpublished g11 experiment data taken from Ref. [5].
  - [37] N. Isgur and G. Karl, Phys. Rev. D **18**, 4187 (1978).
  - [38] A. I. Titov, B. Kampf, S. Date and Y. Ohashi, Phys. Rev. C **72**, 035206 (2005) [Erratum-ibid. C **72**, 049901 (2005)].
  - [39] D. Drechsel, O. Hanstein, S. S. Kamalov and L. Tiator, Nucl. Phys. A **645**, 145 (1999).
  - [40] S. Stepanyan, AIP Conf. Proc. **1257**, 121 (2010).